

Elastoresistivity Signatures of Nematic Fluctuations in Layered Antiferromagnet CoTa_3S_6

Tao Lu,^{1,2} Zili Feng,^{1,2} Mengxing Ye,³ Takashi Kurumaji,^{1,2} and Linda Ye^{1,2,*}

¹*Division of Physics, Mathematics and Astronomy,
California Institute of Technology, Pasadena, CA 91125, USA*

²*Institute of Quantum Information and Matter, California Institute of Technology, Pasadena, CA 91125, USA*

³*Department of Physics and Astronomy, University of Utah, Salt Lake City, UT 84112, USA*

(Dated: March 16, 2026)

Nematic phases that break rotational symmetry are widely observed in quantum materials, and clarifying their origin and relationship with other symmetry-breaking phases remains an important but challenging task. In this work, we investigate nematic fluctuations in CoTa_3S_6 using elastoresistivity experiments to resolve the nature of the proposed nematic phase intertwined with collinear and non-coplanar antiferromagnetic orders. We observe a divergence-like antisymmetric elastoresistivity that rapidly develops below the stripe antiferromagnetic transition, consistent with a distinct nematic degree of freedom coupled to the magnetic order. While nematic fluctuations are strongly modulated by an external out-of-plane magnetic field and the onset temperature of resistivity anisotropy shows pronounced strain dependence, the antiferromagnetic transition temperatures remain nearly unchanged under either magnetic field or strain. Additionally, complementary magnetoresistance measurements reveal characteristic signatures of three-state nematicity in a hexagonal system. Our findings demonstrate CoTa_3S_6 as a unique case of intertwined nematic and AFM orders with distinct origins.

Electronic nematicity refers to a state that spontaneously breaks the discrete lattice rotational symmetries where translational symmetries are preserved. It has emerged as a widespread phenomena in correlated electron systems [1], and frequently found to be intertwined with other ordered phases—such as antiferromagnetism, charge density wave and superconductivity. Historically, nematic phases were first identified in ultra-clean quantum Hall systems [2, 3], while they are later reported to play a key role in iron-based superconductors, where the superconducting dome emerges in the vicinity of the quantum critical points of stripe magnetism and nematic orders, pointing to a close connection between nematicity and unconventional superconductivity [4, 5]. More recently, nematic orders have been reported in more extensive families of quantum materials, including nickel analogues of iron-based superconductors [6], twisted multilayer graphene [7, 8], kagome metals [9–11] and superconductors [4, 12–14], and correlated low dimensional magnets [15–18], motivating a more comprehensive picture of underlying mechanisms leading to the ubiquitous presence of nematic phases across otherwise disparate material platforms.

From an experimental perspective, nematic order is often identified through the emergence of in-plane anisotropy below an ordering temperature in macroscopic probes such as electronic transport [4, 7] and optical response coefficients [11], or alternatively through the observation of rotational-symmetry breaking in momentum-space spectroscopies [9, 10]. However, many

rotational symmetry-breaking patterns are, in principle, also compatible with ordered states that involve additional translational symmetry breaking. A common example is the development of a finite modulation wave vector \mathbf{q} that selects a preferred spatial direction, as realized in stripe magnetic orders [15] and unidirectional charge- or spin-density-wave phases [19, 20]. Indeed, nematic order can be intertwined with such states as a vestigial phase [21], underscoring the need for experimental tools capable of distinguishing genuine nematic order—where rotational symmetry breaking is primary—from spatially modulated phases in which it appears as a secondary consequence. In this context, symmetry-breaking strain, together with associated transport and thermodynamic probes [22–24], has been increasingly established as an effective conjugate field to the nematic order parameter and its fluctuations, owing to the fact that strain breaks identical symmetries as a primary nematic order and thereby couples bilinearly to it. In particular, elastoresistivity has emerged as a powerful technique for detecting nematic fluctuations and for quantitatively characterizing the strain–nematic coupling [6, 22, 25–28].

In this work, we will apply elastoresistivity to explore the nature of a recently reported system to host the nematic order, namely the layered antiferromagnet CoTa_3S_6 . CoTa_3S_6 belongs to a family of magnetic intercalated transition metal dichalcogenides [29–33], and renewed interest in this class of materials has been driven by the discovery of a large anomalous Hall effect within the antiferromagnetic state of CoTa_3S_6 and its isostructural cousin CoNb_3S_6 [34–38]. Two successive magnetic transitions are reported in CoTa_3S_6 at $T_{N1} \approx 37$ K and $T_{N2} \approx 26$ K, with anomalous Hall effect observed below

* lindaye@caltech.edu

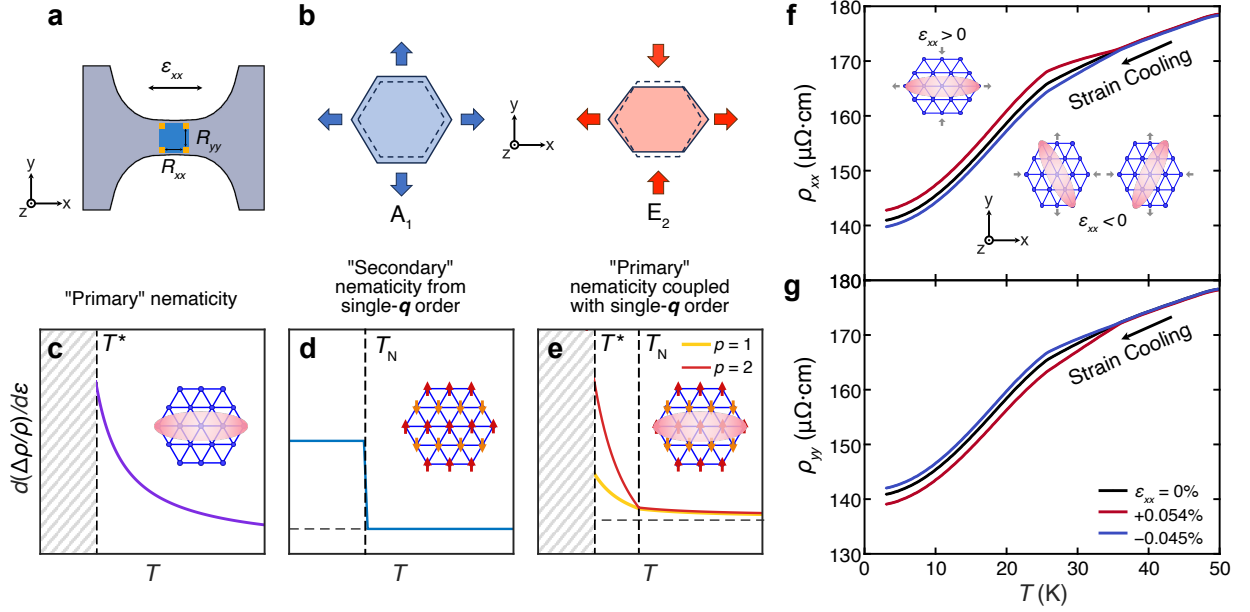


FIG. 1. **Schematics of probing nematic order in CoTa_3S_6 with external strain.** (a) Schematic of the modified Montgomery technique for elastoresistivity measurement. A near square sample with four contacts on the corner is glued onto a titanium platform to apply uniaxial strain along the x -direction, with resistances R_{xx} and R_{yy} measured at the same time, which are converted to resistivities ρ_{xx} and ρ_{yy} (see Methods). (b) Schematic of strain deformations classified by the A_1 (left) and E_2 (right) irreducible representations in the D_6 point group; throughout the work we adopt a Cartesian coordinate system (x, y, z) . (c) Landau-theory-based schematic temperature dependence of nematic susceptibility ($d[\Delta\rho/\rho]/d\epsilon$) for a primary nematicity scenario, where nematicity exists as an independent order parameter. The inset shows the nematic order on the triangular lattice, where the long axis of the red shaded ellipse correspond to the direction along which $\Delta\rho > 0$. (d) Schematic temperature dependence of nematic susceptibility ($d[\Delta\rho/\rho]/d\epsilon$) for a secondary nematicity scenario induced by single- \mathbf{q} (e.g. AFM) order, in which nematicity arises as a “by product” associated with magnetic symmetry breaking. T_N corresponds to the single- \mathbf{q} (e.g. AFM) transition temperature (see text). The inset shows a typical single- \mathbf{q} AFM order on the triangular lattice. (e) Corresponding schematic for a primary nematicity scenario coupled to single- \mathbf{q} (e.g. AFM) order, where $p = 1, 2$ demonstrates the results from different nemato-magnetic coupling strength (see Methods). In this model, we adopt the case where AFM transition temperature T_N is above T^* . Below T^* , hatched area indicates the hysteretic region with multiple nematic domains. (f-g) Temperature dependence of the longitudinal resistivity ρ_{xx} and ρ_{yy} showing strain-cooling-induced selection of nematic domains in CoTa_3S_6 under tensile (red curve) and compressive strain (blue curve), corresponding to the domain configurations illustrated schematically.

T_{N2} [29, 35]. Neutron scattering experiments suggest that the magnetic structure on the Co triangular lattice is a single- \mathbf{q} collinear antiferromagnetic order right below T_{N1} , which then turns into a non-coplanar triple- \mathbf{q} structure below T_{N2} [39–41]. The latter state is expected to host finite scalar spin chirality to account for the topological origin of the observed anomalous Hall effect [39, 40, 42–44]. More recently, in addition to time-reversal symmetry breaking, rotational symmetry breaking is reported in the system, where in-plane resistivity anisotropy and optical birefringence emerge below T_{N1} at $T^* \simeq 34$ K and persist down to low temperature [45]. The appearance of electronic anisotropy at a temperature between T_{N1} and T_{N2} —and its survival into the triple- \mathbf{q} ground state—is unexpected and suggests an origin distinct from the magnetic phase transitions. Clarifying the origin of the anisotropy, and how this anisotropy is related to and distinct from underlying magnetic orders remains an open question that motivates the present study.

Here we carry out a comprehensive elastoresistivity study on CoTa_3S_6 to address the nature of the observed anisotropic nematic order. The experimental configuration is shown in Fig. 1a, where the longitudinal strain ϵ_{xx} along the titanium bridge is controlled experimentally in an in-situ manner with resistivities ρ_{xx} and ρ_{yy} measured simultaneously, allowing one to probe multiple components of the elastoresistivity tensor m_{ij} (see Methods). We note that the strained sample shown in Fig. 1a will be subject to both symmetric (belonging to the A_1 irreducible representation of the D_6 point group) and antisymmetric (belonging to the E_2 irreducible representation of D_6) strain as illustrated in Fig. 1b, allowing one to extract the proper irreducible components of the elastoresistivity tensor m_{A_1} and m_{E_2} (see Methods) where the latter $m_{E_2} = d[(\Delta\rho/\rho)_{xx} - (\Delta\rho/\rho)_{yy}]/d[\epsilon_{xx} - \epsilon_{yy}]$ is expected to be directly capturing the susceptibility and fluctuations of a nematic order that breaks in-plane rotation symmetries. Here $\Delta\rho$ is defined as the devia-

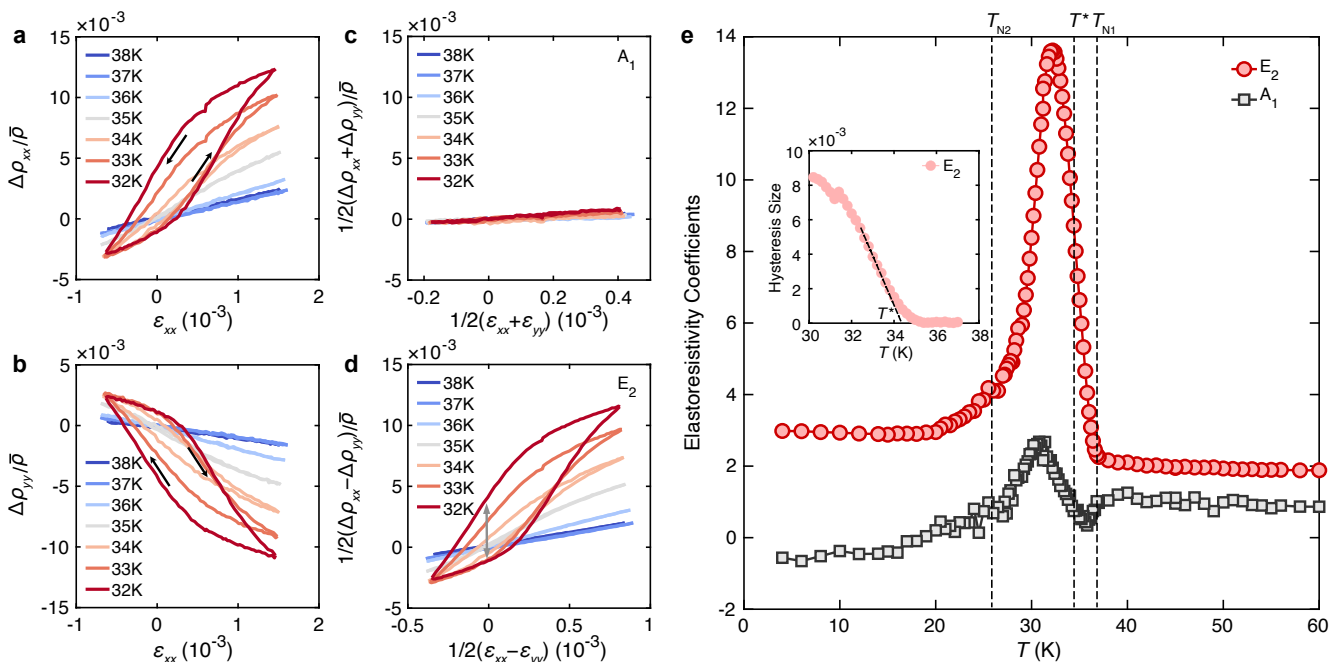


FIG. 2. **Elastoresistivity and nematic susceptibility.** (a-b) Relative changes of resistivity ρ_{ii} ($i = x, y$) as a function of strain (defined as $\Delta\rho_{ii} = \rho_{ii} - \bar{\rho}$) at representative temperatures measured by the modified Montgomery method. $\bar{\rho} = (\rho_{xx,0} + \rho_{yy,0})/2$ is the average in-plane resistivity, where $\rho_{xx,0}$ and $\rho_{yy,0}$ are the resistivity value at $\varepsilon_{xx} = 0$ for the increasing strain scan. The black arrows denote the strain scan direction for the hysteresis loop. (c-d) Representative data of resistivity decomposed to the isotropic A_1 and anisotropic E_2 channels at different temperatures. The gray arrow in (d) defines the size of hysteresis at $\varepsilon = 0$. (e) Temperature dependence of elastoresistivity coefficients (see Methods). Transition temperatures T_{N1} , T^* , T_{N2} are indicated with dashed lines. Inset shows the temperature dependence of hysteresis size of E_2 channel defined in (d) in the resistivity-strain scan. T^* is defined as the onset temperature of hysteresis: intercept of the dashed line with the temperature axis.

tion from the corresponding isotropic resistivity $\bar{\rho}$ with $\Delta\rho_{ii} = \rho_{ii} - \bar{\rho}$.

In Fig. 1c-e, we illustrate three different scenarios for the antisymmetric elastoresistance coefficient $d[\Delta\rho/\rho]/d\varepsilon$ within a Landau free energy framework: a pure nematic order with order parameter η_n (Fig. 1c, with $\Delta\rho/\rho \propto \eta_n$), ‘secondary’ nematicity driven by the emergence of a finite- q vector η_q (Fig. 1d, with $\Delta\rho/\rho \propto \eta_q^2$), and a third scenario where η_n and η_q are distinct primary order parameters which coexist (Fig. 1e, with $\Delta\rho/\rho \propto \eta_n$). The crucial difference among these scenarios is that the leading symmetry-allowed order parameter-strain coupling takes the form $\eta_n \varepsilon$ for a genuine nematic order and the form of $\eta_q^2 \varepsilon$ for the ‘secondary’ rotation symmetry-breaking. In the pure nematic case (Fig. 1c), above the ordering temperature, a Curie-Weiss divergence is expected in $d[\Delta\rho/\rho]/d\varepsilon$ analogous to the magnetic susceptibility near a ferromagnetic order [22, 23, 46]; below the ordering temperature $d[\Delta\rho/\rho]/d\varepsilon$ becomes poorly defined as strain hysteresis onsets. In the second scenario (Fig. 1d), no linear strain-driven anisotropy is expected above the transition (corresponding to $d[\Delta\rho/\rho]/d\varepsilon = 0$), and $d[\Delta\rho/\rho]/d\varepsilon$ shows a step-wise increase at the transition [47, 48]. In the third scenario, aside from the onset

of separate orders, terms in the form of $\eta_q^2 \eta_n$ and $p\eta_q^2 \eta_n \varepsilon$ characterizing the interplay between η_n and η_q are additionally allowed. A sizable $p\eta_q^2 \eta_n \varepsilon$ coupling can lead to a marked increase in the elastoresistivity coefficient below T_N on top of a Curie-Weiss behavior approaching T^* (Fig. 1e, see Methods and Supplementary Materials).

Strain response and elastoresistivity coefficients of CoTa_3S_6 In Fig. 1f(g), we show $\rho_{xx}(\rho_{yy})$ along $a(b^*)$ -axis for a CoTa_3S_6 sample on the strain platform cooled under zero (black), moderate tensile (red) and compressive (blue) ε_{xx} . While both resistivities exhibit negligible strain dependence at high temperatures, a pronounced and opposite strain response in ρ_{xx} and ρ_{yy} emerges below ~ 37 K. This points to the onset of electronic anisotropy upon entering the magnetic/nematic regime and is consistent with strain-controlled nematic domains at low temperatures, as schematically illustrated in the inset of Fig. 1f [45].

In Fig. 2a-b we show normalized $\Delta\rho_{xx}$ and $\Delta\rho_{yy}$ as a function of ε_{xx} , which are largely linear above 37 K, while a finite hysteresis gradually develops upon cooling below $\simeq 34$ K. We attribute the observed hysteresis to the presence of nematic domains at low temperature. After decomposing the elastoresistivity into isotropic A_1 and

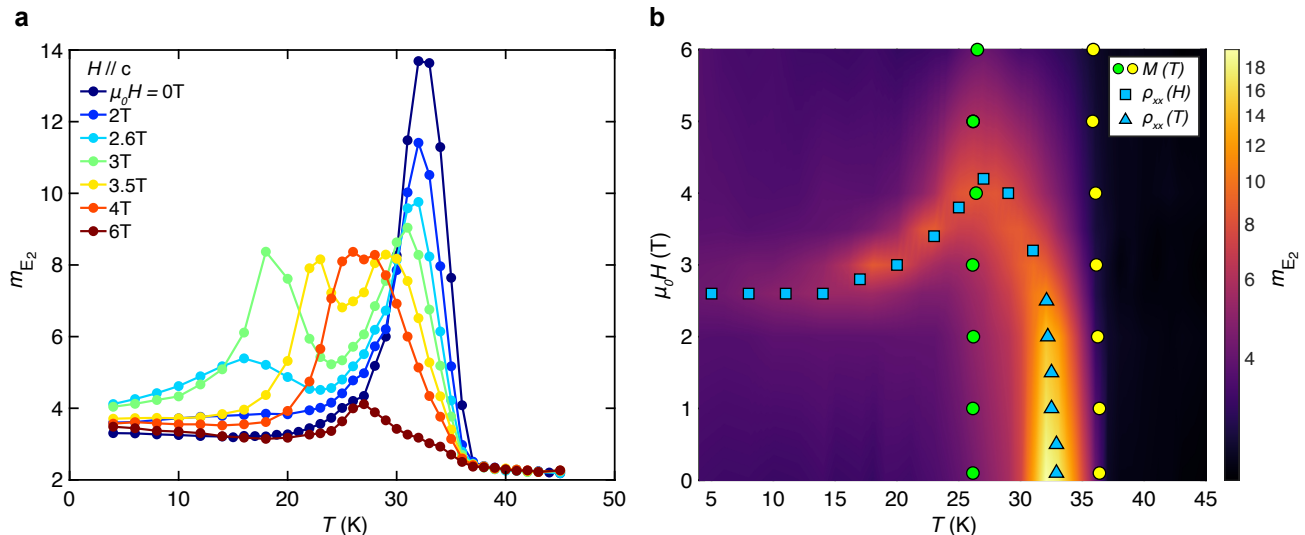


FIG. 3. **Nematic fluctuations controlled by out-of-plane magnetic fields.** (a) Temperature dependence of the elastoresistivity coefficient in the E_2 channel (m_{E_2}), measured under different out-of-plane magnetic fields. (b) Colormap of m_{E_2} in log scale, overlaying with magnetic transition temperatures, illustrating the H - T phase diagram. The phase boundaries T^* (blue triangles), H_c (blue squares), T_{N1} (yellow dots) and T_{N2} (green dots) are indicated by symbols extracted from anomalies in $M(T)$ (circles), $\rho_{xx}(H)$ (squares), and $\rho_{xx}(T)$ (triangles), compiled from previous work [45].

anisotropic E_2 channels (Fig. 2c-d), we find that $\Delta\rho/\bar{\rho}-\epsilon$ is linear at all temperatures in the A_1 channel (Fig. 2c); responses in the E_2 channel (Fig. 2d), in contrast, is highly nonlinear and hysteretic below 35 K. The inset of Fig. 2e summarizes the size of E_2 hysteresis (Fig. 2d) at zero strain in $\Delta\rho/\bar{\rho}$, which allows one to define the onset temperature T^* for the nematic order $T^* \simeq 34$ K, consistent with that determined from magnetic field-trained resistivity [45].

The slopes, namely the corresponding elastoresistivity coefficients, are summarized in Fig. 2e where m_{E_2} are shown as red and m_{A_1} as black symbols, respectively. m_{A_1} exhibits weak temperature dependence over the entire measured temperature range; meanwhile, m_{E_2} is at least one order of magnitude larger and exhibits a pronounced peak around 32 K: this contrast highlights that the dominant strain response of the system lies in the anisotropic E_2 channel, reflecting an underlying rotational symmetry breaking. We note that the temperature evolution of m_{E_2} is rather intriguing: above T_{N1} , m_{E_2} slowly increases with decreasing T ; an upturn occurs at T_{N1} as m_{E_2} approaches T^* divergently. At about 32 K below T^* , m_{E_2} reaches its maximum and subsequently decreases, which we attribute to a progressive freezing and pinning of nematic domains as thermal fluctuations are suppressed. We note that the measured m_{E_2} closely resembles the free energy simulation shown above in Fig. 1e, in contrast to the step-like enhancement at the transition temperature (Fig. 1d) as expected and observed in systems where rotational symmetry is simply broken as a by-product of a spatially varying order. Our observations therefore

rule out a scenario in which the resistivity anisotropy in CoTa_3S_6 is merely a consequence of the collinear, single- q antiferromagnetic order; instead, they are consistent with a primary nematic order that couples bilinearly to external strain which further intertwines with the collinear antiferromagnetic state.

Nematic fluctuations modulated by out-of-plane magnetic field In order to gain additional insights on the interplay between nematicity and the underlying magnetic orders in CoTa_3S_6 , below we trace the effect of c -axis magnetic field to the measured nematic susceptibility m_{E_2} , recalling that previous works reported that the nematic order can be fully suppressed by a moderate out-of-plane magnetic field [45]. Fig. 3a shows $m_{E_2} - T$ under selected out-of-plane magnetic field H : with increasing H , the peak of m_{E_2} is gradually suppressed and shifts towards lower temperatures. Above $\mu_0 H = 2.6$ T, an additional peak develops on the low-temperature side ~ 16 K. The second peak gradually shifts toward higher temperatures with increasing H , and merges with the higher temperature peak at $\mu_0 H \simeq 4$ T. With further increasing H , the overall magnitude of m_{E_2} is suppressed and becomes nearly temperature independent.

Figure 3b presents a color map of m_{E_2} in the $T - H$ plane. The brightest ridge in the color map marks the locations where the nematic fluctuations are strongest. We have overlaid the phase boundaries T_{N1} , T_{N2} and T^* (compiled from previous work [45]) with the color map, where one can see that the nematic fluctuations are strongest at zero field right below T^* , and at finite magnetic fields the enhanced nematic fluctuations

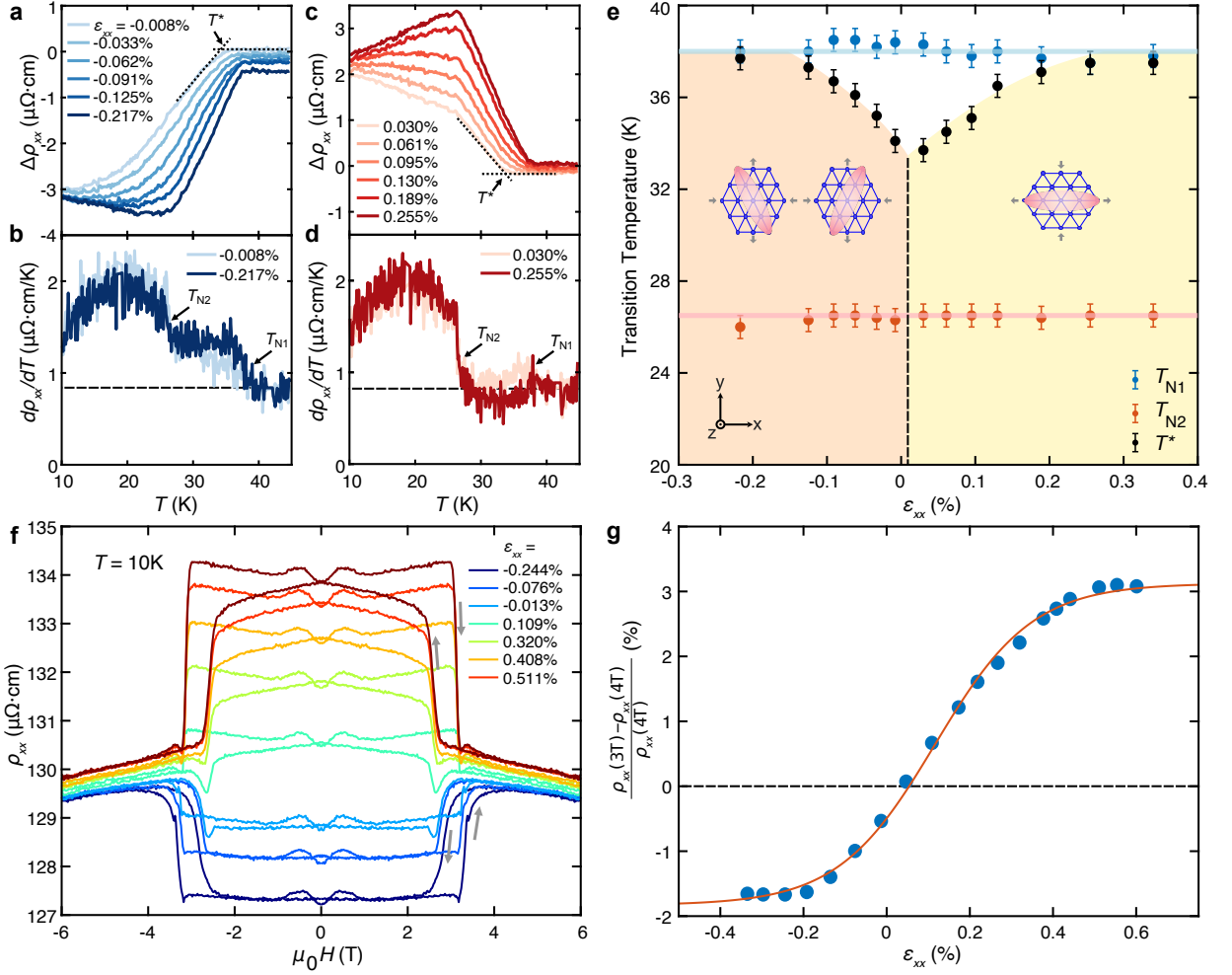


FIG. 4. **Strain dependence of transition temperatures and features of three-state nematicity.** (a,c) Resistivity anisotropy $\Delta\rho_{xx}$ obtained by subtracting a zero strain background from strained states (see Methods), from which T^* under different bias strains is determined. (b,d) Representative $d\rho_{xx}/dT$ curves under bias strains where T_{N1} and T_{N2} are determined from kinks. (e) Summarized strain dependence of the transition temperatures T_{N1} , T_{N2} and T^* . T_{N1} (T_{N2}) under different bias strains fall on the line of $T = 38$ K (blue) ($T = 26.5$ K (red)). Two shaded regions divided by the dashed line indicate the nematic phases with illustrated domains favored by compressive (left) and tensile (right) strains respectively. (f) Out-of-plane magnetic field ($H \parallel z$) dependence of ρ_{xx} measured at 10 K under various magnitudes of strain along the x axis (ϵ_{xx}). (g) Strain dependence of nematic order parameter at each bias strain projected on the x -axis extracted from $(\rho_{xx}(3T) - \rho_{xx}(4T))/\rho_{xx}(4T)$ (see text). The red line is a fit to domain population formula modified for the three-state nematicity (see SI).

directly follows the field-evolution of the phase boundary defined by T^* . That the phase boundary intersects the field axis at $\mu_0 H_c \approx 2.6$ T in the low temperature limit [45] is also captured in constant temperature cuts of m_{E_2} (see SI), and the double peak structure in the T -scans at intermediate magnetic fields is consistent with a non-monotonic T -evolution of H_c . These observations therefore highlight that the nematic fluctuations in CoTa_3S_6 are sensitively captured by elastoresistance and are highly tunable by out-of-plane magnetic field.

Strain evolutions of the nematic order In the following we examine the strain evolution of the nematic and antiferromagnetic critical temperatures T^* , T_{N1} and

T_{N2} . Here T^* is defined via $\Delta\rho_{xx}$ obtained by subtracting a zero strain background $\rho_{xx} - T$ from strained states (see Methods and Fig. 4a and c) while T_{N1} and T_{N2} are determined from kinks in $d\rho_{xx}/dT$ (Fig. 4b and d). We summarize the strain-dependence of T^* , T_{N1} and T_{N2} in Fig. 4e as black, blue and red symbols, respectively. While T_{N1} and T_{N2} remain nearly unchanged over the entire strain range in the study (from -0.3% to $+0.4\%$), the nematic onset temperature T^* exhibits a pronounced ‘V-shape’ strain dependence, which could be attributed to two sets of different strain-selective domains as illustrated in the inset of Fig. 4e. Similar ‘V-shape’ strain dependence for different domains have been reported in multiple systems with rotational sym-

metry breaking [16, 49, 50]. Specifically, T^* increases from ~ 34 K at near-zero bias strain to about 38 K for strains exceeding 0.2% on either the tensile or compressive side, where T^* coincides and appears to merge with T_{N1} .

As CoTa_3S_6 hosts a hexagonal crystalline lattice, the nematic order in the system in principle contains three inequivalent domains and can be mapped onto the three-state Potts model, in contrast to the two-state Ising nematicity in tetragonal systems [4, 27]. Here we present signatures of the three-state nature of the nematicity in CoTa_3S_6 . In Fig. 4f we show ρ_{xx} as a function of out-of-plane magnetic field at $T = 10$ K at selected bias strains. The sign switching of magnetoresistance from tensile (negative) to compressive (positive) strain is consistent with Ref. [45]. Given that at around $\mu_0 H = 3$ T the system evolves from the nematic phase to a C_3 rotational symmetric phase, we quantify the nematic order parameter at each bias strain projected on the x -axis as the jump in ρ_{xx} at H_c : $\Delta\rho_{xx}/\rho_0(H_c)$. This relies on the assumption that the high-field ρ_{xx} provides a good approximation to a corresponding multi-domain, isotropic state at the same bias strain. Specifically, we define $\Delta\rho_{xx}/\rho_0(H_c) \equiv \frac{\rho_{xx}(3\text{T}) - \rho_{xx}(4\text{T})}{\rho_{xx}(4\text{T})}$.

In Fig. 4g we showcase $\Delta\rho_{xx}/\rho_0(H_c)$ as a function of bias strain. For the three state Potts model, the free energy could be written as $F_n = b_0(T - T_n)n^2 + cn^3 \cos 6\theta + wn^4 - \lambda n\epsilon \cos(2\theta - 2\theta_S)$, where $\mathbf{n} = n(\cos\theta, \sin\theta)$ is the nematic order parameter, and λ is its coupling strength to external strain $\boldsymbol{\epsilon} = \epsilon(\cos\theta_S, \sin\theta_S)$. The inequivalence for tensile and compressive strain due to the $cn^3 \cos 6\theta$ term is a key characteristic feature for three-states nematicity, while an Ising nematic system should behave in a symmetric manner on tensile and compressive strains. By minimizing the free energy, we find that the saturation value of $\Delta\rho_{xx}/\rho_0 \propto n \cos 2\theta$ under tensile strain (favoring $\theta = 0$ domains) should be twice that under compressive strain (favoring $\theta = \pi/3, 2\pi/3$ domains, see Supplementary Information), consistent with our observations in Fig. 4g.

Discussion In this work, using anisotropic elastoresistance, we examine the response of intertwined nematic and magnetic orders in CoTa_3S_6 to external (out-of-plane) magnetic fields and uniaxial strains. Our observation of highly field-sensitive nematic fluctuations in elastoresistivity, viewed together with the largely field-independent antiferromagnetic transitions T_{N1} and T_{N2} , suggests that the antiferromagnetic orders (in particular the collinear antiferromagnetic order) are distinct from the nematic order which drives the electronic anisotropy in the system. This scenario is further corroborated by the distinct strain responses of T^* and the magnetic transition temperatures.

The elastoresistivity of CoTa_3S_6 exhibits a distinct

temperature evolution compared to materials in which rotational symmetry breaking is believed to arise as a secondary effect of a single- \mathbf{q} state selecting a preferred spatial direction. A representative hexagonal system is the kagome metal CsV_3Sb_5 , where recent elastoresistance measurements revealed jump-like anomalies in both E_{2g} and A_{1g} channels, with the response dominated by the A_{1g} signal [48, 51]. In that case, the reduced rotational symmetry is interpreted as arising from the stacking pattern of the triple- \mathbf{q} CDW rather than from a primary electronic nematic instability. In contrast, the elastoresistivity response in CoTa_3S_6 evolves continuously below T_{N1} and across T^* , and is best described within a free-energy framework involving a nematic degree of freedom that couples bilinearly to symmetry-breaking strain, with the detailed temperature dependence further influenced by the intertwined magnetic order parameters. More generally, our results illustrate that elastoresistivity, when analyzed within a symmetry-based free-energy framework and combined with controlled tuning parameters such as magnetic field and strain, provides a powerful approach for identifying the origin of rotational symmetry breaking and disentangling intertwined ordered states.

Acknowledgement

The experimental works carried out at Caltech are supported by Gordon and Betty Moore Foundation through Moore Materials Synthesis Fellowship to L.Y. (GBMF12765) and Institute of Quantum Information and Matter (IQIM), an NSF Physics Frontier Center (PHY-2317110). M.Y. is supported by a start-up grant from the University of Utah. M.Y. and L.Y. acknowledge support from the Gordon and Betty Moore Foundation's EPiQS Initiative (Grant GBMF11918), which enabled valuable discussions. Z.F. acknowledges support from IQIM Postdoctoral Fellowship at Caltech. Part of the work at Caltech is carried out at the X-Ray Crystallography Facility supported by the Beckman Institute and at the shared Physical Properties Measurement System facilities supported by NSF DMR-2117094.

METHODS

Crystal Growth and Characterization

Single crystals of CoTa_3S_6 were grown by a two-step process reported in [45]. The typical dimension of the obtained crystals is 1 – 2 mm. The phase purity of the crystals was checked by powder X-ray diffraction, and the orientation of the single crystalline samples was determined by a Laue diffractometer. Energy dispersive X-ray spectroscopy was used to characterize the resulting stoichiometry of the single crystals. It was measured

on the ZEISS 1550VP field emission SEM with Oxford X-Max SDD X-ray Energy Dispersive Spectrometer (EDS) system.

Modified Montgomery Method

The modified Montgomery method is an effective technique for measuring the anisotropic resistivity in orthogonal directions within a single sample simultaneously [51–53]. In this study, CoTa_3S_6 is polished into a thin, nearly square shape with its edges aligned along the x - and y -axes, respectively. Four electrodes were attached at the corners of the sample with relative small contact area to ensure precise measurements. The resistance R_{xx} (R_{yy}) was determined by applying current I_x (I_y) along the x -(y -) axis on one side and measuring the voltage drop V_x (V_y) on the opposite side; and $R_{xx} = V_x/I_x$ ($R_{yy} = V_y/I_y$). The resistivities ρ_{xx} and ρ_{yy} were calculated based on the ratio of R_{xx} and R_{yy} (see the Supplementary Information for details).

Landau Free Energy Modeling

The schematic temperature dependence of nematic susceptibility $d[\Delta\rho/\rho]/d\epsilon$ is modeled within a framework based on Landau theory. For simplicity, we consider a reduced phenomenological model in which the nematic order parameter is projected onto a single component along the selected symmetry-breaking direction ($\theta = 0$). For a primary nematicity scenario, a pure nematic order is described by an order parameter η_n , and the free energy of the system is

$$F_n = \frac{1}{2}a(T - T_0)\eta_n^2 + \frac{1}{4}b\eta_n^4 - g\epsilon\eta_n, \quad (1)$$

Solving $dF_n/d\eta_n = 0$ results in the Curie-Weiss behavior $d\eta_n/d\epsilon \propto g/[a(T - T_0)]$, as plotted in Fig. 1c. Higher-order symmetry-allowed terms (such as cubic terms relevant for three-state nematicity) do not modify the leading Curie-Weiss behavior of the nematic susceptibility and are therefore omitted here for clarity.

For a secondary nematicity scenario from a single- \mathbf{q} order, the order parameter η_q quadratically couples to strain as $\eta_q^2\epsilon$, and

$$F_q = \frac{1}{2}a(T - T_0)\eta_q^2 + \frac{1}{4}b\eta_q^4 - g\epsilon\eta_q^2, \quad (2)$$

Solving $dF_q/d\eta_q = 0$ results in

$$\frac{d(\eta_q^2)}{d\epsilon} = \begin{cases} 0, & T > T_0 \\ 2h/b, & T < T_0 \end{cases}, \quad (3)$$

as plotted in Fig. 1d.

For the case of a primary nematic order coupled to a single- \mathbf{q} order (including the cubic term), the free energy writes:

$$F = b_0(T - T_n)\eta_n^2 + c\eta_n^3 + w\eta_n^4 - (\lambda + p\eta_q^2)\eta_n\epsilon - g\eta_q^2\eta_n, \quad (4)$$

where $\lambda_{eff} = \lambda + p\eta_q^2$ is the renormalized nemato-elastic coupling dependent on the single- \mathbf{q} order (e.g. magnetization), and p reflects the nemato-magnetic coupling strength. The free energy F is minimized with respect to η_n numerically by choosing the values of parameters as follows: $T_n = 30$, $b_0 = 2$, $c = -0.5$, $w = 5$, $\lambda = 10$, $p = 1, 2$, $g = 0.1$, bias strain $\epsilon_{bias} = 0.005$; for the single- \mathbf{q} order, we use the simplest mean-field result $\eta_q^2 = k|T_{N1} - T|$, where $k = 3$ and $T_{N1} = 37$. The resulting $d\eta_n/d\epsilon$ as a function of T is plotted in Fig. 1e.

Transport Measurement under Strain

Electrical transport properties were measured using both standard four-wire methods and modified Montgomery method in the commercial cryostat TeslatronPT (Oxford Instruments) with a superconducting magnet. Strain was applied to single crystals of CoTa_3S_6 using a commercial piezoelectric uniaxial strain cell (CS-100, Razorbill Instruments). For data shown in Fig.2, a near square-shaped sample ($0.80 \times 0.86 \times 0.02 \text{ mm}^3$) is affixed onto a titanium platform in bowtie shape (Fig. 1a, thickness 0.3 mm), which is later attached to CS-100 cell to generate strain (see dedicated section below). For data shown in Fig. 4, a polished bar-shape sample with typical dimension of $1.5 \times 0.68 \times 0.1 \text{ mm}^3$ was mounted to the strain cell with Stycast 2850FT epoxy. The center part of the sample between the mounting plates is approximately 0.7 mm – we assume this to be the length L of the strained region of the sample and it is used to estimate the applied strain through $\epsilon_{xx} = \Delta L/L$ where ΔL is obtained from the capacitive displacement sensor in the strain cell. The piezoelectric stacks were controlled by a combination of the DC output of Keithley 6221 current source and TEGAM 2350 high voltage amplifier. Longitudinal and Hall resistivities were measured using external lock-in amplifiers (Stanford Research Systems, SR860) with an AC current of typical amplitude 2 mA from a voltage controlled current source (Stanford Research Systems, CS580).

Elastoresistivity Tensor in D6 Point Group

Elastoresistivity is a fourth-rank tensor that can be expressed as $m_{ij} = \frac{\partial(\Delta\rho/\rho)_i}{\partial\epsilon_j}$, where i and j take values from 1 to 6 corresponding to xx , yy , zz , yz , zx and xy , following the Voigt notation. These elastoresistivity tensors can be further grouped and decomposed into different

symmetry channels based on the irreducible representation from the crystal lattice point group. In the D_6 point group as in the case of CoTa_3S_6 , the nematic susceptibility corresponds to the elastoresistivity coefficient $m_{E_2} = m_{11} - m_{12}$, and the symmetric mode with A_1 symmetry corresponds to $m_{A_1} = m_{11} + m_{12} - m_{13}[2\nu_{ac}/(1 - \nu_{ab})]$, where $\nu_{ac,ab}$ are the out-of-plane and in-plane Poisson ratios respectively. A near square-shaped sample is affixed onto a titanium platform in bowtie shape, which is later attached to a piezoelectric strain cell (CS-100, Razorbill) to apply uniaxial strain onto the sample and generate a combination of anisotropic $\frac{1}{2}(\epsilon_{11} - \epsilon_{12})$ and isotropic $\frac{1}{2}(\epsilon_{11} + \epsilon_{12})$ strain components. We use the modified Montgomery methods to measure ρ_{xx} and ρ_{yy} simultaneously and extract the strain-induced change in resistivity $d[(\Delta\rho/\rho)_{xx}]/d\epsilon_{xx}$ and $d[(\Delta\rho/\rho)_{yy}]/d\epsilon_{xx}$ from the linear fitting of $(\Delta\rho_{xx}/\bar{\rho}) - \epsilon_{xx}$ (Fig. 2a) and $(\Delta\rho_{yy}/\bar{\rho}) - \epsilon_{xx}$ (Fig. 2b) scans. In the hysteretic region, the resistance values from the two scan directions at the same strain are averaged before performing a linear fit over the strain range from -0.04% to $+0.12\%$. And the corresponding elastoresistivity tensors are calculated using the following formula:

$$\begin{aligned} m_{E_2} &= \frac{d[(\Delta\rho/\rho)_{xx} - (\Delta\rho/\rho)_{yy}]}{d[\epsilon_{xx} - \epsilon_{yy}]} \\ &= \frac{1}{1 + \nu_p} \frac{d[(\Delta\rho/\rho)_{xx} - (\Delta\rho/\rho)_{yy}]}{d\epsilon_{xx}}, \end{aligned} \quad (5)$$

$$\begin{aligned} m_{A_1} &= \frac{d[(\Delta\rho/\rho)_{xx} + (\Delta\rho/\rho)_{yy}]}{d[\epsilon_{xx} + \epsilon_{yy}]} \\ &= \frac{1}{1 - \nu_p} \frac{d[(\Delta\rho/\rho)_{xx} + (\Delta\rho/\rho)_{yy}]}{d\epsilon_{xx}}. \end{aligned} \quad (6)$$

Here $\nu_p \approx 0.33$ is approximated as the Poisson ratio of the titanium platform since the sample is much thinner.

Resistivity Anisotropy under Applied Bias Strains

The resistivity anisotropy (proxy for nematic order parameter) as a function of temperature under different bias strains in Fig. 4a and c are taken in the following sequence. The system is cooled across T^* with no external strain and no magnetic field applied. Then a warming scan of $\rho_{xx}(T)$ from 10 K to 45 K is recorded and use this as the zero-strain background. To prepare a state with finite macroscopic nematic order parameter, the sample is first cooled from 45 K to 10 K with no strain applied. Then the out-of-plane magnetic field is set to 6 T at 10 K, much above the critical field that restores the rotational symmetry. Then an external tensile (compressive) strain $\epsilon_{xx} \approx +0.2\%$ ($\epsilon_{xx} \approx -0.2\%$) is applied before magnetic field sweeping back to 0 T. This

process is defined as an in-situ strain training assisted by the field-induced transition at H_c (see SI), which is better than selecting the domain by cooling the system with an external strain (more precisely, a fixed voltage on the piezo stack), because the latter would substantially shift the zero-strain condition due to the temperature- and voltage-history dependence of the Razorbill piezo stack. After this in-situ strain training process, we get states with populated domains favored by tensile (compressive) strains for Fig. 4a (Fig. 4c) after the external strain is removed at $\mu_0 H = 0$ T. Then the external strain ϵ_{xx} is set to one of the target values as shown in the legend for Fig. 4a and c, and a warming curve of $\rho_{xx}(T)$ is taken with the strain applied. After that, the $\Delta\rho_{xx}(T)$ curve under this specific external strain is obtained by subtracting the zero-strain background, and thus directly represents the temperature evolution of the nematic order parameter under the bias strain.

AUTHOR CONTRIBUTIONS

T.L. performed elastoresistivity measurements and strain experiments. Z.F. grew the single crystals and conducted initial characterization. T.L. carried out free-energy modeling and numerical simulation with M.Y. and L.Y.. The experiments were designed, and the results were analyzed through discussions among T.L., T.K., and L.Y.. T.L., T.K., and L.Y. wrote the manuscript with input from all authors.

DATA AVAILABILITY

The datasets generated during and/or analyzed during the current study will be available in the Caltech Research Data Repository when the manuscript is published.

COMPETING INTERESTS

The authors declare no competing interests.

-
- [1] E. Fradkin, S. A. Kivelson, M. J. Lawler, J. P. Eisenstein, and A. P. Mackenzie, Nematic fermi fluids in condensed matter physics, *Annu. Rev. Condens. Matter Phys.* **1**, 153 (2010).
 - [2] M. P. Lilly, K. B. Cooper, J. P. Eisenstein, L. N. Pfeiffer, and K. W. West, Evidence for an anisotropic state of two-dimensional electrons in high landau levels, *Physical Review Letters* **82**, 394 (1999).
 - [3] R. R. Du, D. C. Tsui, H. L. Stormer, L. N. Pfeiffer, K. W. Baldwin, and K. W. West, Strongly anisotropic trans-

- port in higher two-dimensional Landau levels, *Solid State Communications* **109**, 389 (1999).
- [4] J.-H. Chu, J. G. Analytis, K. De Greve, P. L. McMahon, Z. Islam, Y. Yamamoto, and I. R. Fisher, In-plane resistivity anisotropy in an underdoped iron arsenide superconductor, *Science* **329**, 824 (2010).
 - [5] R. M. Fernandes, A. V. Chubukov, and J. Schmalian, What drives nematic order in iron-based superconductors?, *Nat. Phys.* **10**, 97 (2014).
 - [6] C. Eckberg, D. J. Campbell, T. Metz, J. Collini, H. Hodovanets, T. Drye, P. Zavalij, M. H. Christensen, R. M. Fernandes, S. Lee, P. Abbamonte, J. W. Lynn, and J. Paglione, Sixfold enhancement of superconductivity in a tunable electronic nematic system, *Nat. Phys.* **16**, 346 (2020).
 - [7] Y. Cao, D. Rodan-Legrain, J. M. Park, N. F. Q. Yuan, K. Watanabe, T. Taniguchi, R. M. Fernandes, L. Fu, and P. Jarillo-Herrero, Nematicity and competing orders in superconducting magic-angle graphene, *Science* **372**, 264 (2021).
 - [8] R. M. Fernandes and J. W. F. Venderbos, Nematicity with a twist: Rotational symmetry breaking in a moiré superlattice, *Sci. Adv.* **6**, eaba8834 (2020).
 - [9] H. Li, S. Cheng, B. R. Ortiz, H. Tan, D. Werhahn, K. Zeng, D. Johrendt, B. Yan, Z. Wang, S. D. Wilson, and I. Zeljkovic, Electronic nematicity without charge density waves in titanium-based kagome metal, *Nat. Phys.* **19**, 1591 (2023).
 - [10] C. Farhang, W. R. Meier, W. Lu, J. Li, Y. Wu, S. Mozafari, R. P. Madhugaria, Y. Zhang, D. Mandrus, and J. Xia, Discovery of an intermediate nematic state in a bilayer kagome metal ScV_6Sn_6 , *Nature Communications* **16**, 7867 (2025).
 - [11] Y. Xu, Z. Ni, Y. Liu, B. R. Ortiz, Q. Deng, S. D. Wilson, B. Yan, L. Balents, and L. Wu, Three-state nematicity and magneto-optical Kerr effect in the charge density waves in kagome superconductors, *Nat. Phys.* **18**, 1470 (2022).
 - [12] A. E. Böhrer, J.-H. Chu, S. Lederer, and M. Yi, Nematicity and nematic fluctuations in iron-based superconductors, *Nature Physics* **18**, 1412 (2022).
 - [13] R. A. Borzi, S. A. Grigera, J. Farrell, R. S. Perry, S. J. S. Lister, S. L. Lee, D. A. Tennant, Y. Maeno, and A. P. Mackenzie, Formation of a nematic fluid at high fields in $\text{Sr}_3\text{Ru}_2\text{O}_7$, *Science* **315**, 214 (2007).
 - [14] V. Hinkov, D. Haug, B. Fauqué, P. Bourges, Y. Sidis, A. Ivanov, C. Bernhard, C. T. Lin, and B. Keimer, Electronic liquid crystal state in the high-temperature superconductor $\text{YBa}_2\text{Cu}_3\text{O}_{6.45}$, *Science* **319**, 597 (2008).
 - [15] A. Little, C. Lee, C. John, S. Doyle, E. Maniv, N. L. Nair, W. Chen, D. Rees, J. W. Venderbos, R. M. Fernandes, *et al.*, Three-state nematicity in the triangular lattice antiferromagnet $\text{Fe}_{1/3}\text{NbS}_2$, *Nat. Mater.* **19**, 1062 (2020).
 - [16] K. Hwangbo, E. Rosenberg, J. Cenker, Q. Jiang, H. Wen, D. Xiao, J.-H. Chu, and X. Xu, Strain tuning of vestigial three-state Potts nematicity in a correlated antiferromagnet, *Nat. Phys.* **20**, 1888 (2024).
 - [17] Q. Tan, C. A. Occhialini, H. Gao, J. Li, H. Kitadai, R. Comin, and X. Ling, Observation of three-state nematicity and domain evolution in atomically thin antiferromagnetic NiPS_3 , *Nano Letters* **24**, 7166 (2024).
 - [18] W. Yao, V. P. Antonio, D. Adroja, S. J. G. Alvarado, B. Gao, S. Xu, R. Liu, X. Lu, and P. Dai, Signatures of three-state Potts nematicity in spin excitations of the van der Waals antiferromagnet FePSe_3 (2025), arXiv:2509.02475.
 - [19] X. Chen, J. L. Schmehr, Z. Islam, Z. Porter, E. Zoghlin, K. Finkelstein, J. P. C. Ruff, and S. D. Wilson, Unidirectional spin density wave state in metallic $(\text{Sr}_{1-x}\text{La}_x)_2\text{IrO}_4$, *Nature Communications* **9**, 103 (2018).
 - [20] Y. Guo, M. Klemm, J. S. Oh, Y. Xie, B.-H. Lei, L. Moreschini, C. Chen, Z. Yue, S. Gorovikov, T. Pedersen, M. Michiardi, S. Zhdanovich, A. Damascelli, J. Denlinger, M. Hashimoto, D. Lu, C. Jozwiak, A. Bostwick, E. Rotenberg, S.-K. Mo, R. G. Moore, J. Kono, R. J. Birgeneau, D. J. Singh, P. Dai, and M. Yi, Spectral evidence for unidirectional charge density wave in detwinned BaNi_2As_2 , *Physical Review B* **108**, L081104 (2023).
 - [21] R. M. Fernandes, P. P. Orth, and J. Schmalian, Intertwined vestigial order in quantum materials: Nematicity and beyond, *Annu. Rev. Condens. Matter Phys.* **10**, 133 (2019).
 - [22] J.-H. Chu, H.-H. Kuo, J. G. Analytis, and I. R. Fisher, Divergent nematic susceptibility in an iron arsenide superconductor, *Science* **337**, 710 (2012).
 - [23] A. E. Böhrer, J.-H. Chu, S. Lederer, and M. Yi, Nematicity and nematic fluctuations in iron-based superconductors, *Nature Physics* **18**, 1412 (2022).
 - [24] M. S. Ikeda, T. Worasaran, E. W. Rosenberg, J. C. Palmstrom, S. A. Kivelson, and I. R. Fisher, Elastocaloric signature of nematic fluctuations, *Proceedings of the National Academy of Sciences* **118**, e2105911118 (2021).
 - [25] H.-H. Kuo, M. C. Shapiro, S. C. Riggs, and I. R. Fisher, Measurement of the elastoresistivity coefficients of the underdoped iron arsenide $\text{Ba}(\text{Fe}_{0.975}\text{Co}_{0.025})_2\text{As}_2$, *Physical Review B* **88**, 085113 (2013).
 - [26] H.-H. Kuo, J.-H. Chu, J. C. Palmstrom, S. A. Kivelson, and I. R. Fisher, Ubiquitous signatures of nematic quantum criticality in optimally doped Fe-based superconductors, *Science* **352**, 958 (2016).
 - [27] E. W. Rosenberg, J.-H. Chu, J. P. C. Ruff, A. T. Hristov, and I. R. Fisher, Divergence of the quadrupole-strain susceptibility of the electronic nematic system YbRu_2Ge_2 , *Proceedings of the National Academy of Sciences* **116**, 7232 (2019).
 - [28] M. Frachet, P. Wiecki, T. Lacmann, S. M. Souliou, K. Willa, C. Meingast, M. Merz, A.-A. Haghighirad, M. Le Tacon, and A. E. Böhrer, Elastoresistivity in the incommensurate charge density wave phase of $\text{BaNi}_2(\text{As}_{1-x}\text{P}_x)_2$, *Npj Quantum Mater.* **7**, 1 (2022).
 - [29] S. Parkin and R. Friend, *3d* transition-metal intercalates of the niobium and tantalum dichalcogenides. I. magnetic properties, *Philos. Mag. B* **41**, 65 (1980).
 - [30] T. Miyadai, K. Kikuchi, H. Kondo, S. Sakka, M. Arai, and Y. Ishikawa, Magnetic properties of $\text{Cr}_{1/3}\text{NbS}_2$, *J. Phys. Soc. Jpn.* **52**, 1394 (1983).
 - [31] E. Morosan, H. Zandbergen, L. Li, M. Lee, J. Checkelsky, M. Heinrich, T. Siegrist, N. P. Ong, and R. Cava, Sharp switching of the magnetization in $\text{Fe}_{1/4}\text{TaS}_2$, *Phys. Rev. B* **75**, 104401 (2007).
 - [32] S. Wu, Z. Xu, S. C. Haley, S. F. Weber, A. Acharya, E. Maniv, Y. Qiu, A. A. Aczel, N. S. Settinieri, J. B. Neaton, *et al.*, Highly tunable magnetic phases in transition-metal dichalcogenide $\text{Fe}_{1/3+\delta}\text{NbS}_2$, *Phys. Rev. X* **12**, 021003 (2022).
 - [33] L. S. Xie, S. Husremovic, O. Gonzalez, I. M. Craig, and D. K. Bediako, Structure and magnetism of iron-and

- chromium-intercalated niobium and tantalum disulfides, *J. Am. Chem. Soc.* **144**, 9525 (2022).
- [34] N. J. Ghimire, A. S. Botana, J. S. Jiang, J. Zhang, Y.-S. Chen, and J. F. Mitchell, Large anomalous hall effect in the chiral-lattice antiferromagnet CoNb_3S_6 , *Nat. Commun.* **9**, 3280 (2018).
- [35] P. Park, Y.-G. Kang, J. Kim, K. H. Lee, H.-J. Noh, M. J. Han, and J.-G. Park, Field-tunable toroidal moment and anomalous hall effect in noncollinear antiferromagnetic weyl semimetal $\text{Co}_{1/3}\text{TaS}_2$, *npj Quantum Materials* **7**, 42 (2022).
- [36] S. Mangelsen, P. Zimmer, C. Näther, S. Mankovsky, S. Polesya, H. Ebert, and W. Bensch, Interplay of sample composition and anomalous hall effect in Co_xNbS_2 , *Phys. Rev. B* **103**, 184408 (2021).
- [37] G. Tenasini, E. Martino, N. Ubrig, N. J. Ghimire, H. Berger, O. Zaharko, F. Wu, J. F. Mitchell, I. Martin, L. Forró, and A. F. Morpurgo, Giant anomalous hall effect in quasi-two-dimensional layered antiferromagnet $\text{Co}_{1/3}\text{NbS}_2$, *Phys. Rev. Res.* **2**, 023051 (2020).
- [38] H. Tanaka, S. Okazaki, K. Kuroda, R. Noguchi, Y. Arai, S. Minami, S. Ideta, K. Tanaka, D. Lu, M. Hashimoto, *et al.*, Large anomalous hall effect induced by weak ferromagnetism in the noncentrosymmetric antiferromagnet CoNb_3S_6 , *Phys. Rev. B* **105**, L121102 (2022).
- [39] P. Park, W. Cho, C. Kim, Y. An, Y.-G. Kang, M. Avdeev, R. Sibille, K. Iida, R. Kajimoto, K. H. Lee, *et al.*, Tetrahedral triple-q magnetic ordering and large spontaneous hall conductivity in the metallic triangular antiferromagnet $\text{Co}_{1/3}\text{TaS}_2$, *Nat. Commun.* **14**, 8346 (2023).
- [40] H. Takagi, R. Takagi, S. Minami, T. Nomoto, K. Ohishi, M.-T. Suzuki, Y. Yanagi, M. Hirayama, N. D. Khanh, K. Karube, and Y. Tokura, Spontaneous topological hall effect induced by non-coplanar antiferromagnetic order in intercalated van der waals materials, *Nat. Phys.* **19**, 961 (2023).
- [41] P. Park, W. Cho, C. Kim, Y. An, K. Iida, R. Kajimoto, S. Matin, S.-S. Zhang, C. D. Batista, and J.-G. Park, Contrasting dynamical properties of single-Q and triple-Q magnetic orderings in a triangular lattice antiferromagnet (2024), arXiv:2410.02180 [cond-mat.str-el].
- [42] Y. Yanagi, H. Kusunose, T. Nomoto, R. Arita, and M.-T. Suzuki, Generation of modulated magnetic structures based on cluster multipole expansion: Application to α -Mn and CoM_3S_6 , *Phys. Rev. B* **107**, 014407 (2023).
- [43] H. Park and I. Martin, DFT+ DMFT study of the magnetic susceptibility and the correlated electronic structure in transition-metal intercalated NbS_2 , *Phys. Rev. B* **109**, 085110 (2024).
- [44] O. Heinonen, R. Heinonen, and H. Park, Magnetic ground states of a model for MNb_3S_6 ($M = \text{Co}, \text{Fe}, \text{Ni}$), *Phys. Rev. Materials* **6**, 024405 (2022).
- [45] Z. Feng, W. Lu, T. Lu, F. Liu, J. R. Sheeran, M. Ye, J. Xia, T. Kurumaji, and L. Ye, Nonvolatile nematic order manipulated by strain and magnetic field in a layered antiferromagnet (2025), arXiv:2507.05486 [cond-mat.str-el].
- [46] S. C. Riggs, M. C. Shapiro, A. V. Maharaj, S. Raghu, E. D. Bauer, R. E. Baumbach, P. Giraldo-Gallo, M. Wartenbe, and I. R. Fisher, Evidence for a nematic component to the hidden-order parameter in URu_2Si_2 from differential elastoresistance measurements, *Nature Communications* **6**, 6425 (2015).
- [47] B. Lüthi, *Physical Acoustics in the Solid State* (Springer Science & Business Media, 2007).
- [48] K. Sun, L. Nie, H. Li, J. Zhao, H. Rao, F. Yu, M. Shi, Z. Xiang, J. Ying, Z. Wang, T. Wu, and X. Chen, Intertwined charge density wave order in vanadium based kagome superconductors (2025).
- [49] J. A. W. Straquadine, M. S. Ikeda, and I. R. Fisher, Evidence for realignment of the charge density wave state in ErTe_3 and TmTe_3 under uniaxial stress via elastocaloric and elastoresistivity measurements, *Phys. Rev. X* **12**, 021046 (2022).
- [50] L. Ye, Y. Sun, V. Sunko, J. F. Rodriguez-Nieva, M. S. Ikeda, T. Worasaran, M. E. Sorensen, M. D. Bachmann, J. Orenstein, and I. R. Fisher, Elastocaloric signatures of symmetric and antisymmetric strain-tuning of quadrupolar and magnetic phases in $\text{dyb}2\text{c}2$, *Proc. Natl. Acad. Sci. U.S.A.* **120**, e2302800120 (2023).
- [51] Z. Liu, Y. Shi, Q. Jiang, E. W. Rosenberg, J. M. DeStefano, J. Liu, C. Hu, Y. Zhao, Z. Wang, Y. Yao, *et al.*, Absence of E_{2g} nematic instability and dominant A_{1g} response in the kagome metal CsV_3Sb_5 , *Phys. Rev. X* **14**, 031015 (2024).
- [52] H. Montgomery, Method for measuring electrical resistivity of anisotropic materials, *J. Appl. Phys.* **42**, 2971 (1971).
- [53] C. Dos Santos, A. De Campos, M. Da Luz, B. White, J. Neumeier, B. De Lima, and C. Shigue, Procedure for measuring electrical resistivity of anisotropic materials: A revision of the montgomery method, *J. Appl. Phys.* **110** (2011).